Heat and Mass Transfer Modeling of Dry Gases in the Cathode of PEM Fuel Cells

M.J. Kermani[1*] **J.M. Stockie**[2†]

[1] Department of Mechanical Engineering

[2] Department of Mathematics and Statistics

University of New Brunswick

Fredericton, NB, Canada, E3B 5A3

SUMMARY

The transport of three gas species, O_2, H_2O and N_2, through the cathode of a proton exchange membrane (PEM) fuel cell is studied numerically. The diffusion of the individual species is modeled via the Maxwell-Stefan equations, coupled with appropriate conservation equations. Two mechanisms are assumed for the internal energy sources in the system: a volumetric heat source due to the electrical current flowing through the cathode; and heat flow toward the cathode at cathode-membrane interface due to the exothermic chemical reaction at this interface, in which water is generated. The governing equations of the unsteady fluid motion are written in fully conservative form, and consist of the following: (i) three equations for the mass conservation of the species; (ii) the momentum equation for the mixture, which is approximated using Darcy's Law for flow in porous media; and (iii) an energy equation, written in a form that has enthalpy as the dependent variable.

Keywords: PEM fuel cells; Maxwell-Stefan equations; Finite volume method; Porous media; Non-reacting mixtures

1 INTRODUCTION

Zero emission power generation has always been the ideal goal of people in the power generation community. One approach to achieve this goal is via proton exchange membrane (PEM) fuel cells, which in principle combine oxygen and hydrogen gas in a reaction that generates electrical current, producing only water as a byproduct. A PEM fuel cell consists of two electrodes, the anode (hydrogen supply source) and the cathode (oxygen supply source), between which is sandwiched a polymer membrane, usually consisting of Nafion®. The interfaces between the electrodes and membrane are impregnated with a platinum catalyst, as depicted in Fig. 1.

*Corresponding author, Post Doctoral Fellow, Department of Mechanical Engineering, Fax: ++1 (702) 974 9307, M.Kermani@unb.ca

†Assistant Professor, Department of Mathematics and Statistics.

Approximate position of Fig. 1.

A great deal of recent research has appeared in the literature on modeling of transport processes in PEM fuel cells. The vast majority of work (for example Gurau et al. (1998), Singh et al. (1999) and Yi and Nguyen (1999)) has focused on mass transport and it is only more recently that more complete models including heat transport and condensation have appeared (see He et al. (2000), Rowe and Li (2001) and Wang et al. (2001)).

The present work is part of an ongoing effort to carefully model individual elements of the PEM fuel cell, with a particular focus on simulation of the flow of gas in the porous electrodes. The transport of two species in both anode and cathode was studied by Promislow and Stockie (2001), and this work was extended in Stockie et al. (2003) to handle three species, with $(1, 2, 3) = (H_2, H_2O, CO_2)$ in the anode and $(1, 2, 3) = (O_2, H_2O, N_2)$ in the cathode. These two previous papers assumed isothermal conditions prevailed in the flow domain, whereas an extension of the model to temperature-dependent flows recently performed by Bradean et al. (2001), in which the two-species diffusion was governed by Fick's Law and temperature was used as the dependent variable in the energy equation.

In this paper, we present a model for gas transport in the cathode that is similar to that developed by Bradean et al. (2001), except that the full Maxwell-Stefan equations are used for diffusion and enthalpy is used as the independent variable in the energy equation. Our motivation for using enthalpy is that it is a more appropriate quantity for capturing the physics of condensation, which will play an important role in future modeling efforts. First, we validate the numerical model against several isothermal and temperature-dependent test cases reported in the literature. Then, the temperature-dependent algorithm is applied to a three-species flow. In the present work, there is no liquid water, but regions of possible condensation can be identified by considering locations where the partial pressure of H_2O hypothetically exceeds the steam saturation pressure at the mixture temperature.

2 MATHEMATICAL MODELING

2.1 Governing Equations

The governing equations for unsteady flow of a gas mixture composed of three species, $(1, 2, 3) = O_2$, H_2O and N_2, are described here. Three equations for the mass conservation of the species are required, along with momentum and energy equations for the mixture. The momentum equation is approximated by Darcy's Law for flow in porous media, and the energy equation is written in terms of enthalpy in order to simplify future extension of this work to include water condensation.

The conservation equation for the mixture mass can be written as:

$$\frac{\partial \rho}{\partial t} + \nabla \cdot \left[\rho \vec{V}\right] = 0, \tag{1}$$

where ρ and $\vec{V}$ are the mixture density and velocity. For species 1 and 2, the conservation equations are:

$$\frac{\partial C_1}{\partial t} + \nabla \cdot \overbrace{\left[C_1 \vec{V} + \vec{J_1}\right]}^{N_1} = 0, \tag{2}$$

$$\frac{\partial C_2}{\partial t} + \nabla \cdot \underbrace{\left[C_2 \vec{V} + \vec{J_2}\right]}_{N_2} = 0, \tag{3}$$

where C_1 and C_2 indicate species molar concentration, and N_1 and N_2 represent the total species fluxes (advective + diffusive). It is important to note that the molar diffusive fluxes $\vec{J_1}$ and $\vec{J_2}$ are measured relative to the mass-averaged velocity $\vec{V}$.

A simplified form of the momentum equation, Darcy's Law for porous media, is assumed to hold in the porous electrode:

$$\vec{V} = -\frac{K}{\epsilon \mu} \nabla P, \tag{4}$$

where μ is the mixture viscosity, and K (permeability) and ϵ (porosity) are characteristics of the porous media.

The energy equation can be written in terms of total enthalpy, $H = h + \frac{V^2}{2}$ as:

$$\frac{\partial}{\partial t} \left(\rho H - P \right) + \nabla \cdot \left[\rho \vec{V} H\right] = -\nabla \cdot \vec{q} + \dot{q}_s \tag{5}$$

where we are operating under low speed conditions in which the work of shear stress is ignored. The flux term $\vec{q}$ arises from two effects, conductive heat flux and diffusive enthalpy fluxes for the multi-species gas mixture, and so can be written as

$$\vec{q} = -\kappa \nabla T + \sum_{i=1}^{3} h_i \, \vec{j_i} = -\kappa \nabla T + \sum_{i=1}^{3} \bar{h}_i \, \vec{J_i}. \tag{6}$$

The specific enthalpy of species i is denoted by h_i, and the mass diffusion flux relative to the mass-averaged velocity by $\vec{j_i} = \rho_i(\bar{V_i} - \vec{V})$, where $\bar{V_i}$ is the velocity of species i, $\vec{V}$ (as noted before) is the mass-averaged mixture velocity, and hence $(\bar{V_i} - \vec{V})$, relative velocity of the species i w.r.t. the mixture velocity, is the diffusion velocity of species i. The second form of the diffusive enthalpy term in Eqn. (6) can be derived by making use of the definitions $\bar{h}_i = M_i h_i$ for the molar specific enthalpy and $\vec{J_i} = C_i(\bar{V_i} - \vec{V})$ for the molar diffusive flux relative to the mass-averaged velocity. In Eqn. (5), $\dot{q}_s$ is a volumetric heat source arising from ohmic heat generation

$$\dot{q}_s = \frac{i^2}{\sigma} \tag{7}$$

where i is the electrical current density in the electrode and σ is the electrical conductivity.

For flow in fuel cells, speeds are relatively low and so the kinetic energy is several orders of magnitude smaller than the static enthalpy term. Therefore, $H = h + V^2/2 \approx h$, where

$$h = \frac{\bar{h}}{M} = \frac{\sum_{i=1}^{3} Y_i \, \bar{h}_i}{\sum_{i=1}^{3} Y_i \, M_i}, \tag{8}$$

with M being the mixture molecular weight and Y_i the species mole fraction determined by

$$Y_1 = \frac{C_1}{C}, \quad Y_2 = \frac{C_2}{C}, \quad Y_3 = 1 - Y_1 - Y_2. \tag{9}$$

Assuming that all species obey the perfect gas law, in which specific heats can be taken constant near the operating temperature, we then have

$$h = \frac{\left[Y_1 \bar{C}_{p_1} + Y_2 \bar{C}_{p_2} + Y_3 \bar{C}_{p_3}\right] T}{Y_1 M_1 + Y_2 M_2 + Y_3 M_3} \equiv \bar{C}_{p_{av}} T/M \tag{10}$$

Numerical experiments show that the contribution of the second term in Eqn. (6), the diffusive enthalpy flux of the species, is negligible. Ignoring this term, the energy equation for low speed cases reduces to:

$$\frac{\partial}{\partial t}\left(\rho h - P\right) + \nabla \cdot \left[\rho \vec{V} h\right] = \nabla \cdot \left(\kappa \nabla T\right) + \frac{i^2}{\sigma} \tag{11}$$

To close the system of equations, we assume that the mixture obeys the ideal gas law

$$P = C R_0 T, \tag{12}$$

where R_0 is the universal gas constant. The mixture and species concentrations are related via

$$\rho = \sum_{k=1}^{3} \rho_k = C_1 M_1 + C_2 M_2 + M_3 C_3, \tag{13}$$

where $C_3 = [C - C_1 - C_2]$ or

$$C = \left[\rho + \left(M_3 - M_1\right) C_1 + \left(M_3 - M_2\right) C_2\right] / M_3. \tag{14}$$

The auxiliary equations needed to determine the diffusive fluxes, $\vec{J}_1$ and $\vec{J}_2$, are explained in the next section.

2.2 Diffusive Fluxes

The diffusive fluxes, $\vec{J}_k$, are often derived in a simplified form based on Fick's law, which is strictly valid only for mixtures containing two species (see Taylor and Krishna (1993)). A more appropriate model for multi-species diffusion is obtained using the Maxwell-Stefan equations:

$$\begin{bmatrix} \vec{J}_1^* \\ \vec{J}_2^* \end{bmatrix} = -C \underbrace{\begin{bmatrix} D_{11} & D_{12} \\ D_{21} & D_{22} \end{bmatrix}}_{D} \begin{bmatrix} \nabla\left(C_1/C\right) \\ \nabla\left(C_2/C\right) \end{bmatrix}, \tag{15}$$

where C is the mixture concentration, D is the diffusivity matrix of Maxwell-Stefan, and $\vec{J}_k^*$ represents the molar diffusive fluxes relative to the mole-averaged velocity. Each component of the D matrix depends on the binary diffusivity (i.e. Δ_{12}, Δ_{13}, or Δ_{23}), via the relationships

$$\begin{aligned} D_{11} &= \Delta_{13}\left(Y_1 \Delta_{23} + \left(1 - Y_1\right)\Delta_{12}\right)/S, \\ D_{12} &= Y_1 \Delta_{23}\left(\Delta_{13} - \Delta_{12}\right)/S, \\ D_{21} &= Y_2 \Delta_{13}\left(\Delta_{23} - \Delta_{12}\right)/S, \\ D_{22} &= \Delta_{23}\left(Y_2 \Delta_{13} + \left(1 - Y_2\right)\Delta_{12}\right)/S, \end{aligned} \tag{16}$$

where

$$S = Y_1 \Delta_{23} + Y_2 \Delta_{13} + Y_3 \Delta_{12}. \tag{17}$$

The diffusive fluxes based on mole- and mass-averaged velocities, i.e. $\vec{J}_i^*$ and $\vec{J}_i$, are connected via the following relationship (see Taylor and Krishna (1993)):

$$\begin{bmatrix} \vec{J}_1 \\ \vec{J}_2 \end{bmatrix} = S \begin{bmatrix} \vec{J}_1^* \\ \vec{J}_2^* \end{bmatrix} \equiv \begin{bmatrix} s_{11} & s_{12} \\ s_{21} & s_{22} \end{bmatrix} \begin{bmatrix} \vec{J}_1^* \\ \vec{J}_2^* \end{bmatrix}, \tag{18}$$

where the components of the conversion matrix S are

$$s_{kl} = \delta_{kl} - \frac{C_k M_l}{\rho}\left(1 - \frac{M_3}{M_l}\right), \quad k,l = 1,2, \tag{19}$$

where δ is Kronecker delta function, i.e. for $k = l$, $\delta_{kl} = 1$, and $k \neq l$, $\delta_{kl} = 0$.

Combining Eqns. (15) and (18) yields:

$$\begin{bmatrix} \vec{J}_1 \\ \vec{J}_2 \end{bmatrix} = - \begin{bmatrix} a & b \\ c & d \end{bmatrix} \begin{bmatrix} \nabla\left(C_1/C\right) \\ \nabla\left(C_2/C\right) \end{bmatrix}, \tag{20}$$

where

$$\begin{aligned} a &= C\left[s_{11}D_{11} + s_{12}D_{21}\right] \\ b &= C\left[s_{11}D_{12} + s_{12}D_{22}\right] \\ c &= C\left[s_{21}D_{11} + s_{22}D_{21}\right] \\ d &= C\left[s_{21}D_{12} + s_{22}D_{22}\right]. \end{aligned} \tag{21}$$

The final diffusivity matrix D is scaled by a factor of $\epsilon^{1.5} \approx 0.636$, known as a Bruggeman correction, in order to take into account the resistance to diffusion due to the porous medium.

2.3 Discretization of Governing Equations

Obtaining velocity from the Darcy's Law,

$$\vec{V} = -\underbrace{\frac{K}{\epsilon\mu}}_{B_0} \nabla P \equiv -B_0 \nabla P \tag{22}$$

and substituting into Eqns. (1), (2), (3) and (11) yields:

$$\frac{\partial \rho}{\partial t} = \nabla \cdot \left(\, \rho B_0 \, \nabla P \,\right), \tag{23}$$

$$\frac{\partial C_1}{\partial t} = \nabla \cdot \left[\, C_1 B_0 \nabla P - \vec{J}_1 \,\right], \tag{24}$$

$$\frac{\partial C_2}{\partial t} = \nabla \cdot \left[\, C_2 B_0 \nabla P - \vec{J}_2 \,\right], \tag{25}$$

$$\frac{\partial}{\partial t}\left(\rho h - P\right) = \nabla \cdot \left(\rho B_0 h \nabla P\right) + \nabla \cdot \left(\kappa \nabla T\right) + \frac{i^2}{\sigma}. \tag{26}$$

The above equations are discretized using a cell-vertex finite volume approach, in which all flow parameters are stored at cell vertices. This approach allows us to locate nodes on the boundaries of the computational domain. In the description that follows, we represent a typical temporal derivative term by $\partial Q/\partial t$, and spatial derivatives by $\partial F/\partial x$, where F is of the form $F = A(\partial B/\partial x)$ in all cases. Time derivatives are integrated using a first

order explicit scheme, while spatial derivatives are discretized via second order centered differences, suitable for the diffusion terms:

$$\left(\frac{\partial F}{\partial x}\right)_{j,k} = \frac{1}{\Delta x}\left[F_E - F_W\right], \tag{27}$$

where F_E, and F_W are the numerical fluxes at the East (E) and West (W) faces of a control volume surrounding node (j,k). F_E and F_W are determined from

$$F_E = \frac{1}{2\Delta x}\left[A_{j+1,k} + A_{j,k}\right]\left[B_{j+1,k} - B_{j,k}\right], \tag{28}$$

$$F_W = \frac{1}{2\Delta x}\left[A_{j,k} + A_{j-1,k}\right]\left[B_{j,k} - B_{j-1,k}\right], \tag{29}$$

and similarly for the y-derivative terms. As an example, the discretized form of Eqn. 23 could be written as:

$$\frac{Q^{n+1}_{(j,k)} - Q^{n}_{(j,k)}}{\Delta t} = \frac{1}{\Delta x}\left[F_E - F_W\right] + \frac{1}{\Delta y}\left[G_N - G_S\right] \tag{30}$$

where $Q \equiv \rho$,

$$\begin{aligned} F_E &= \left[\, \rho\, B_0\, \frac{\partial P}{\partial x} \,\right]_E , \quad \text{and} \\ G_N &= \left[\, \rho\, B_0\, \frac{\partial P}{\partial y} \,\right]_N . \end{aligned} \tag{31}$$

Similar form for the discretization of Eqns. 24–26 could be used. For the current explicit computation, a globally constant time step for temporal integrations were used. Stability requirements limits the explicit time step to be small enough allowing to capture the physics of transient flow and observe flow acceleration as the solution evolves toward steady-state. The intermediate solutions would only be physically correct, if a physically correct initial condition is provided to the solver.

2.4 Boundary Conditions

For the following discussion of boundary conditions, refer to Fig. 1.

- At boundary locations (I), the wall is assumed to be impermeable. That is, $J^y_1 = J^y_2 = 0$, and $v = 0$, where J^y_k and v represent diffusive flux and velocity components in vertical direction. The heat flux conducted through this boundary is determined by an equivalent convective heat flux from the coolant, written as $-\kappa(\partial T/\partial y) = K^W_T(T^W - T)$, where K^W_T is an equivalent convective heat transfer coefficient between the electrode and coolant, and T^W is the coolant temperature.

- At open channel boundary (II), the gas pressure is set equal to the channel pressure, $P = \bar{P}$. The diffusive fluxes at this boundary are assumed to obey an analogue of Newton's cooling law in heat transfer, i.e. $J^y_k = r^k_0(\bar{C}_k - C_k)$, for $k = 1, 2$, where r^k_0 is the convective mass transfer coefficient for species k. The energy equation at this boundary is approximated by $-\kappa\,(\partial T/\partial y) = K^C_T(\bar{T} - T)$, where K^C_T is the convective heat transfer coefficient in the channel and $\bar{T}$ is the channel temperature.

- At the catalyst boundary (III), species 1 (Oxygen) is assumed to obey the mass flux condition $J_1^y = r_H(C_1 - C_\infty)$, where r_H is the convective mass transfer coefficient, and C_∞ is the concentration at the membrane, usually taken equal to zero. Water vapor (species 2) is generated at this boundary at the rate of two moles of water for each mole of oxygen that crosses the cathode-catalyst boundary; hence, $N_2^y = -2N_1^y$. The inert gas component, species 3 (N_2), cannot penetrate the membrane which is impermeable to gas, and so $N_3^y = 0$. A heat flux arises at this boundary due to the heat of reaction, and hence $\kappa(\partial T/\partial y) = 2N_1^y h_r$, where h_r is the enthalpy of formation of water in gas form.

- At side boundaries (IV), periodic boundary conditions are specified.

3 RESULTS AND DISCUSSIONS

3.1 Numerical Validation

In this section, we present three validating test cases in a fuel cell cathode. This is followed by a full three-species non-isothermal computation in Section 3.2.

3.1.1 Three-species isothermal computation

The first validating test case performed relates to isothermal flow of a three species $(1, 2, 3) = (O_2, H_2O, N_2)$ mixture in the cathode, governed by Eqns. (23) – (25). The computational domain is depicted in Fig. 2.

Comparisons are extremely difficult to do because of the lack of experimental data in the literature. So we have compared to previous published numerical results instead. An isothermal computation reported by Stockie et al. (2003) is used for the comparison purposes, in which the governing equations were discretized using a method of lines, resulted to a system of ordinary differential equations and integrated implicitly using the stiff ODE solver of DASSL.

This computation domain is performed based on the parameters: permeability $K = 10^{-8}\ cm^2$, porosity $\epsilon = 0.74$, viscosity $\mu = 2.24 \times 10^{-4}\ g/(cm.s)$, binary diffusivity coefficients $\Delta_{12} = 0.124$, $\Delta_{13} = 0.104$ and $\Delta_{23} = 0.123\ cm^2/s$, channel pressure $\bar{P} = 1.0 \times 10^6\ dyne/cm^2$, species mole fractions in the channel $Y_1 = 0.21$, $Y_2 = 0.10$ and $Y_3 = 0.69$, channel temperature $\bar{T} = 346.15^o K$, and mass transfer coefficients $r_0^1 = r_0^2 = 10\ cm/s$ and $r_H = 0.8\ cm/s$.

Approximate position of Fig. 2.

Approximate position of Fig. 3.

Approximate position of Fig. 4.

Figures 3 and 4 display the results of the present computation at steady-state for oxygen and water fluxes at the catalyst layer (i.e., the top boundary). The difference in molar fluxes at the peaks or valleys differ by at most 7.1%. The agreement in mole fractions is considerably better, lying within about 1%.

Approximate position of Fig. 5.

In the present computation, neither phase change nor condensation is modeled. However, the regions in which condensation are likely to occur can still be estimated as follows. Condensation occurs at the dew point, where the partial pressure of water vapor, P_v, reaches the saturation pressure at the mixture temperature, i.e. $P_v/P_{sat}(T) \rightarrow 1$. With this in mind, we obtain relative humidity, $\Phi = P_v/P_{sat}(T)$, where the saturation pressure, P_{sat}, is determined from Appendix A, at the mixture temperature. $\Phi < 1$ represents dry regions, and while Φ cannot exceed 1 in an actual condensation problem, we identify regions in which condensation is occurring by $\Phi \geq 1$ in the present dry computations. It is estimated that regions of $\Phi \geq 1$ in isothermal computation cannot provide a reliable knowledge on the locus of wet regions. However, $\Phi \geq 1$ regions in non-isothermal computation (in which energy equation is also solved) can provide quite useful information on the locus of wet regions, and it is estimated these regions can well match with those in a two-phase modeling. This is especially true if equilibrium thermodynamic model is used in a two-phase flow computation, in which moisture onsets as soon as the saturation line is crossed. But in order to evaluate the quantity of generated moisture a non-isothermal dry flow computation is not sufficient and a two-phase flow modeling is required.

Under usual fuel cell operating conditions, liquid water is known to be generated, but the exact location where condensation occurs is unknown. If water condenses on or near the catalyst layer (where the product H_2O enters the cathode), then pockets of water may collect which could potentially narrow the channels through which oxygen gas is supplied to the catalyst. In turn, these pockets of water could restrict or interrupt the supply of oxygen to the catalyst and thereby degrade fuel cell performance. As a result, management of liquid water is of prime importance in fuel cells, and identifying the locus $\Phi = 1$ is a first step in locating potential problem situations.

Figure 5 shows the condensation pockets predicted by the isothermal simulation, which occur at the catalyst boundary. Clearly, the supply of reactant gases are not cut off in this case, but there is a potential for performance degradation if excessive water is generated in these pockets, which could cause regions of the catalyst to be starved of oxygen.

3.1.2 Two-species non-isothermal computation

In the present validating test case, we consider the full set of governing equations, including the energy equation, Eqn. (26). This section deals with a non-isothermal computation of two-species flow (i.e. O_2, H_2O) in the cathode, corresponding to an example considered by Bradean et al. (2001). In their computation, the governing equations were written in steady form, and a pressure-based scheme of Patankar (1980) was employed to iterate on the solution until convergence is obtained. Furthermore, a single-channel geometry was studied (see Fig. 6). It should also be noted that in their computations, the two-species mixture was assumed to obey Fick's Law; our model, on the other hand, has three gas species modeled by the Maxwell-Stefan, and so we have set the concentration of the third species, N_2, to zero in the channel for comparison purposes.

The problem parameters used in this case are as follows: permeability $K = 10^{-8}\ cm^2$, porosity $\epsilon = 0.74$, viscosity $\mu = 2.24 \times 10^{-4}\ g/(cm.s)$, effective diffusivity $D = 0.08\ cm^2/s$ (obtained based on binary diffusivity values of $\Delta_{12} = 0.124$, $\Delta_{13} = 0.104$, and $\Delta_{23} = 0.123\ cm^2/s$), effective thermal conductivity $\kappa = 4. \times 10^5\ erg/(s\ cm\ ^oK)$, specific heat of the mixture $C_p = 2. \times 10^7\ erg/(g\ ^oK)$, channel pressure $\bar{P} = 1.1 \times 10^6\ dyne/cm^2$, mass fraction of O_2 $\rho_{O_2}/\rho = 0.71$ (instead of mass fraction an equivalent mole fraction values of $Y_1 = 0.58$, $Y_2 = 0.42$, and $Y_3 = 0$ are used), channel and coolant temperatures $\bar{T} = T^W = 353.15^oK$, channel mass transfer coefficient $r_0^1 = 800\ cm/s$, channel convective heat transfer coefficient $K_T^C = 1.5 \times 10^4\ erg/(s\ cm^2\ ^oK)$, equivalent convective heat transfer coefficient in graphite $K_T^W = 1.1{\times}10^7\ erg/(s\ cm^2\ ^oK)$, heat of reaction $h_r = 1.36 \times 10^{12}\ erg/mol$, mass transfer coefficient at the catalyst $r_H = 0.3\ cm/s$, and $\dot{q}_s = 0$.

Approximate position of Fig. 6.

Approximate position of Fig. 7.

Approximate position of Fig. 8.

The numerical results for this example are displayed in Figs. 7 and 8. The computed temperatures agree to within approximately 0.6^oK (out of a full range of $\approx 360^oK$). The sources for this slight disagreement (0.16% difference) could be associated to the use of Fickian law in the two-species modeling by Bradean et al. (2001). This is as opposed to the present modeling, in which Maxwell-Stefan has been used. It is noted that in the present computation the mole fraction of the inert gas (Nitrogen), i.e. Y_3, in the channel has been set to zero in order to match the test case of Bradean et al. (2001), however, an infinitesimal non-zero value are calculated as a part of solution for Y_3 throughout the computational domain. The location of the possible condensation region, as depicted in Fig. 8, also matches very well with the results reported by Bradean et al. (2001).

3.1.3 Three-species isothermal; another validating case

As the last validation for the present computation, comparisons will be made with the computation of Um et al. (2000). Figure 9 shows the schematic of cathode and channel in Um et al. (2000) computation. As shown in this figure three-species flow enters the channel at the station (i) and exits at (e). The comparisons will be made at the cross-section $S - S$, which is located at the mid-length of the channel, i.e. $X = L/2$.

The computation is performed based on the data provided by Um et al. (2000). At station (i), on dry basis air molar analysis is 21% oxygen and 79% nitrogen, where relative humidity of Φ =100% is specified. The specified channel pressure is 5 atm (= 5.066 bar), and the computation is performed isothermally at $T = 353^oK(80^oC)$.

To further match the cases, the following parameters are used for permeability $K = 1.76 \times 10^{-7}\ cm^2$, and porosity $\epsilon = 0.4$. The rest of parameters are taken similar to that of Section 3.1.1.

For comparison purpose, the profile of oxygen mole fraction in the cross-section $S - S$ are presented (see Figs. 9 and 10). It should be noted that in the present one-dimensional computation, the values of $Y_1 = 0.171$, and $Y_2 = 0.0935$ have been specified for the channel values of mole fraction. As shown in Fig. 10 the agreement between the test cases are good. The root mean square (RMS) of the difference between the computations have been calculated, giving a value of within 4% difference between the present computation and that of Um et al. (2000). As a further validation, the general trends are consistent with those predicted by the one-dimensional model of Bernardi and Verbrugge (1991).

Approximate position of Fig. 9.

Approximate position of Fig. 10.

3.2 Three-Species Non-Isothermal Computation

In this section, we present simulations of a full three-species non-isothermal flow, and compare the results to an equivalent isothermal calculation. The problem parameters used in this non-isothermal case are: $\kappa = 0.677 \times 10^5 erg/(cm\ s\ ^oK)$, $\bar{C}_{p_{O_2}}$, $\bar{C}_{p_{H_2O}}$, $\bar{C}_{p_{N_2}}$ respectively = 2.97×10^8, 3.39×10^8, and $2.91 \times 10^8\ erg/(mol.^oK)$, $K_T^C = 1.5 \times 10^5\ erg/(s\ cm^2\ ^oK)$, $K_T^W = 1.1 \times 10^7\ erg/(s\ cm^2\ ^oK)$, $T^W = 346.15^oK$, $h_r = 2.418 \times 10^{12}\ erg/mol$, $i = 1.0\ amp/cm^2$, and $\sigma = 7.273 \times 10^{-5}\ amp^2\ s/(erg\ cm)$. The rest of parameters were similar to the test case of Section 3.1.1.

Approximate position of Fig. 11.

Approximate position of Fig. 12.

The $\Phi = 1$ contour in Fig. 11 shows that the electrode remains almost totally dry except for a small pocket of condensation that appears at the bottom boundary above the landing area (the solid wall region separating the two channels). This prediction runs contrary to the results from the isothermal case, in which condensing pockets appear along the top boundary (see Figs. 5 and 11). This significant change in the location of the condensing regions highlights the importance of solving the energy equation along with the other transport equations.

The two sets of results are compared in Fig. 12 along horizontal cross-sections at both the upper and lower boundaries. Figures 12-a, and b show the distribution of the relative humidity, Φ, along the top and bottom boundaries, where $\Phi = P_v/P_{sat}$ and P_{sat} is given by Eqn. (32). Uniform temperature in the isothermal case corresponds to a constant value of saturation pressure. In the non-isothermal case, the temperature field is significantly elevated via two sources: (i) heat source terms, arising from $\dot{q}_s$ in the energy equation; and (ii) the heat of reaction at the catalyst boundary which enters the electrode from the top boundary. The heat of reaction requires that the temperature at the catalyst boundary be the highest along any horizontal cross-section, as evidenced in Fig. 12-f. Furthermore, a maximum temperature variation of about 8.0^oK was obtained along the vertical cross-section at mid-channel ($x = 0.25$ cm). While this temperature variation seems somewhat large in view of the $0.5\ mm$ thickness of the electrode, a milder temperature variation could be obtained, for example, by choosing a material with higher thermal conductivity. A test case has been performed using $\kappa = 4 \times 10^5\ erg/(cm\ s\ ^oK)$ (about 6 times larger thermal conductivity) and a temperature variation of less than 1.0^oK was obtained across the electrode.

We can also use the results of Fig. 12 to explain why the condensing regions migrate from the upper catalyst boundary to the bottom boundary. In Fig. 12-f, the temperature variation along the vertical cross-section $x = 0.5\ cm$ is approximately 5.0^oK, which translates into a rise of $\Delta P_{sat} = 6.21 \times 10^4\ dyne/cm^2$ (about 17% of local saturation pressure). This ΔP_{sat} is the main reason that Φ decreases as we move upward through the electrode above the landing area. It is noted that the main variation in Φ is due to P_{sat}, because of the similarity between mole fraction (Y_2) and mixture pressure (P) between the isothermal and non-isothermal cases (see Figs. 12-c, d, i, and j).

4 CONCLUSION

A mathematical model is presented for simulating isothermal flow of three gas species (O_2, H_2O and N_2) in the cathode of a proton exchange membrane fuel cell. The three transport equations for the three species are augmented by an energy equation in order to determine the temperature variations in the electrode. Regions of possible condensation are obtained using this model by monitoring the over-saturated regions. We demonstrate that only slight variations in temperature throughout the domain (of about 5.0^oK) can significantly change the location of

regions of condensing gas.

Over-saturated regions ($\Phi \geq 1$) in isothermal computations cannot provide a reliable knowledge of the location of liquid water. However, regions where $\Phi \geq 1$ in non-isothermal computations (in which energy equation is also solved) can provide useful information about the wet regions. This is especially true if the equilibrium thermodynamic model is used in a two-phase flow computation, in which condensation occurs as soon as the saturation line is crossed. In order to measure the amount of moisture generated, a more sophisticated model, which includes phase change, is required. We plan to incorporate this change in the future using an equilibrium thermodynamic model.

The energy equation is written in terms of enthalpy or could be written in terms of internal energy (rather than temperature) as the dependent variable, which will be an important issue in future studies that focus on careful modeling of condensation.

Acknowledgment

This research was supported by an NSERC operating grant, and by a research grant from Ballard Power Systems through the MITACS Network of Centres of Excellence.

APPENDIX A

The saturation pressure for steam, within a temperature range of $T = [40, 160]^o C$, is determined from the following polynomial of degree 5 in terms of *dyne/cm*^{2}:

$$P_{_{sat}}(T) = a\,T^5 + b\,T^4 + c\,T^3 + d\,T^2 + e\,T + f, \tag{32}$$

where

$$a = 7.79E - 6, \quad b = +1.06E - 2, \quad c = -9.84E - 1$$
$$d = 1.13E + 2, \quad e = -3.43E + 3, \quad f = +6.60E + 4$$

Thermodynamic data is taken from steam thermodynamic tables of the text by Moran and Shapiro (2000) and fitted using a fifth-order, least squares polynomial approximation.

References

Bernardi, D. M. and Verbrugge (1991) “Mathematical Model of a Gas Diffusion Electrode Bonded to a Polymer Electrolyte”, *AIChE J.* **37** (8) 1151–1163.

Bradean, R. P., Promislow, K., and Wetton, B. R. “Heat and Mass Transfer in Porous Fuel Cell Electrodes” (2001) In *Proceedings of the International Symposium on Advances in Computational Heat Transfer*, Queensland, Australia, May 2001.

Gurau, V., Liu, H., and Kakaç, S. (1998) “Two-Dimensional Model for Proton Exchange Membrane Fuel Cells”, *AIChE J.* **44** (11) 2410–2422.

He, W., Yi, J. S., and Nguyen, T. V. (2000) “Two-Phase Flow Model of the Cathode of PEM Fuel Cells Using Interdigitated Flow Fields”, *AIChE J.* **46** (10) 2053–2064.

Moran, M. J., and Shapiro, H. N. (2000) Fundamentals of Engineering Thermodynamics, Fourth Edition, John Wiley & Sons, Inc..

Patankar, S. V. (1980) Numerical Heat Transfer and Fluid Flow, Hemisphere, Washington DC.

Promislow, K., and Stockie, J. M. (2001) “Adiabatic Relaxation of Convective-Diffusive Gas Transport in a Porous Fuel Cell Electrode”, *SIAM J. Appl. Math.* **62** (1) 180–205.

Rowe, A., and Li, X. (2001) “Mathematical Modeling of Proton Exchange Membrane Fuel Cells”, *J. Power Sources* **102** 82–96.

Singh, D., Lu, D. M., and Djilali, N. (1999) “A Two-Dimensional Analysis of Mass Transport in Proton Exchange Membrane Fuel Cells”, *Internat. J. Eng. Sci.* **37** 431–452.

Stockie, J. M., Promislow, K. and Wetton, B. R. (2003) “A Finite Volume Method for Multicomponent Gas Transport in a Porous Fuel Cell Electrode”, International Journal for Numerical Methods in Fluids, in press.

Taylor, R., and Krishna, R. (1993) Multicomponent Mass Transfer, John Wiley and Sons, New York.

Um, S., Wang, C. Y. and Chen, K. S. (2000) “Computational Fluid Dynamics Modeling of Proton Exchange Membrane Fuel Cells”, *J. Electrochem. Soc.* **147** 4485–4493.

Wang, Z. H., Wang, C. Y., and Chen, K. S. (2001) “Two-Phase Flow and Transport in the Air Cathode of Proton Exchange Membrane Fuel Cells”, *J. Power Sources* **94** (1) 40–50.

Yi J. S., and Nguyen, T. V. (1999) “Multicomponent Transport in Porous Electrodes of Proton Exchange Membrane Fuel Cells Using the Interdigitated Gas Distributors”, *J. Electrochem. Soc.* **146** (1) 38–45.

Figure Captions

1. Figure 1: A schematic picture of a proton exchange membrane (PEM) fuel cell.
2. Figure 2: Computational domain, consisting of a 2D slice through the cathode over a pair of flow channels.
3. Figure 3: Comparison of molar fluxes at the catalyst boundary (the top boundary) for species $(1, 2) = (\mathrm{O}_2, \mathrm{H}_2\mathrm{O})$.
4. Figure 4: Comparison of computed mole fractions at the catalyst boundary (the top boundary) for species $(1, 2, 3) = (\mathrm{O}_2, \mathrm{H}_2\mathrm{O}, \mathrm{N}_2)$.
5. Figure 5: Regions of possible condensation predicted by the model, assuming isothermal conditions.
6. Figure 6: Fuel cell used by Bradean et al. (2001).
7. Figure 7: Comparison of temperature distribution at the catalyst boundary (the top boundary) with the results of Bradean et al. (2001).
8. Figure 8: Region of possible condensation predicted by the present two-species non-isothermal computation with one channel.
9. Figure 9: Cathode and channel schematics in Um et al. (2000) computation.
10. Figure 10: Comparison of oxygen mole fraction (Y_1) across the porous media of cathode, at the cross-section $S - S$ of the previous figure.
11. Figure 11: Region of possible condensation predicted by the present three-species non-isothermal computation with two channel.
12. Figure 12: Comparison of three-species isothermal (left) and non-isothermal (right) computations.

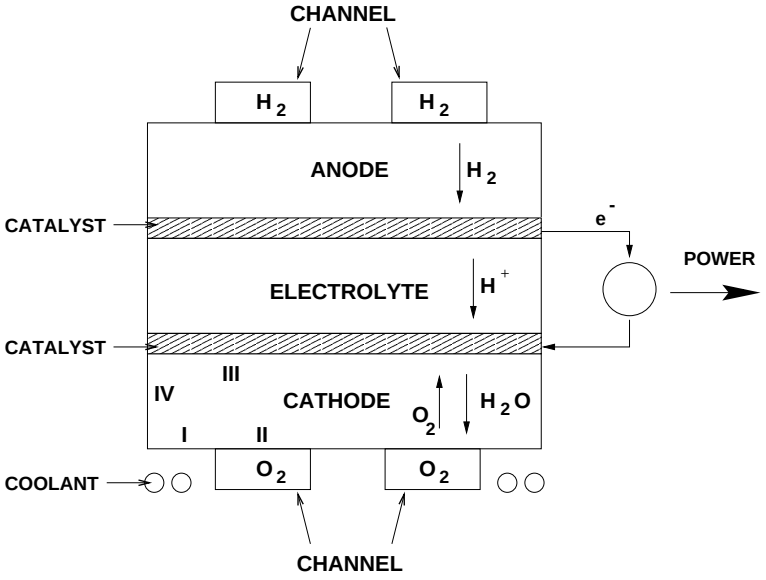

Figure 1: A schematic picture of a proton exchange membrane (PEM) fuel cell.

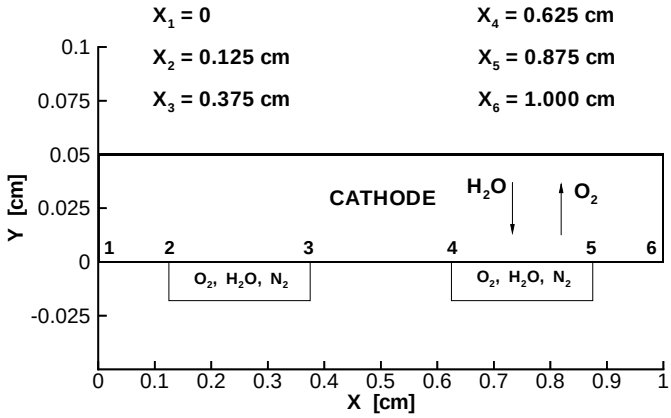

Figure 2: Computational domain, consisting of a 2D slice through the cathode over a pair of flow channels.

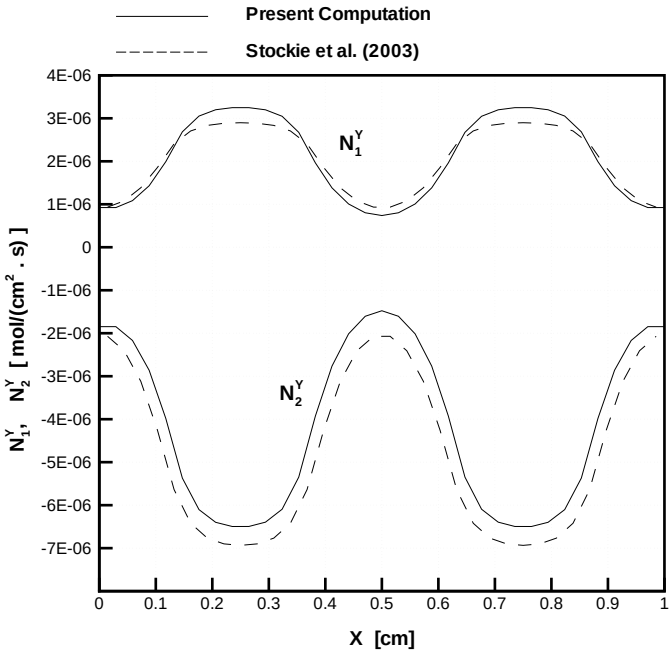

Figure 3: Comparison of molar fluxes at the catalyst boundary (the top boundary) for species $(1, 2) = (\mathrm{O}_2, \mathrm{H}_2\mathrm{O})$.

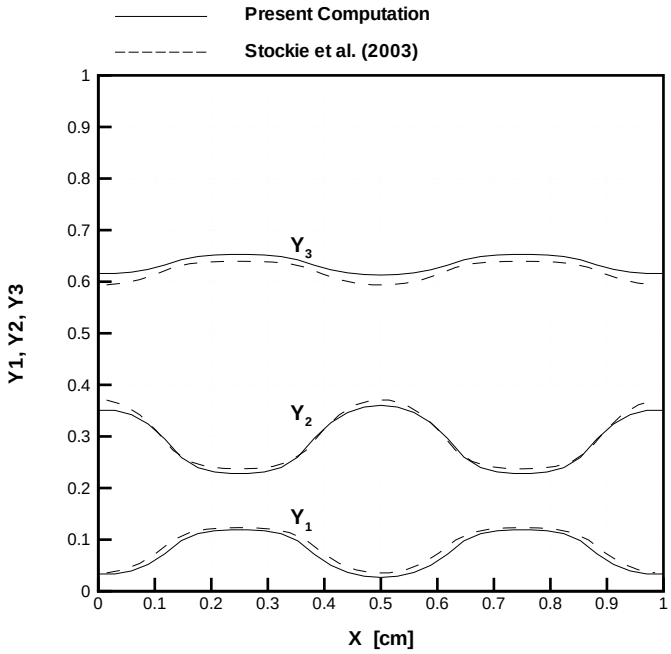

Figure 4: Comparison of computed mole fractions at the catalyst boundary (the top boundary) for species $(1, 2, 3) = (\mathrm{O}_2, \mathrm{H}_2\mathrm{O}, \mathrm{N}_2)$.

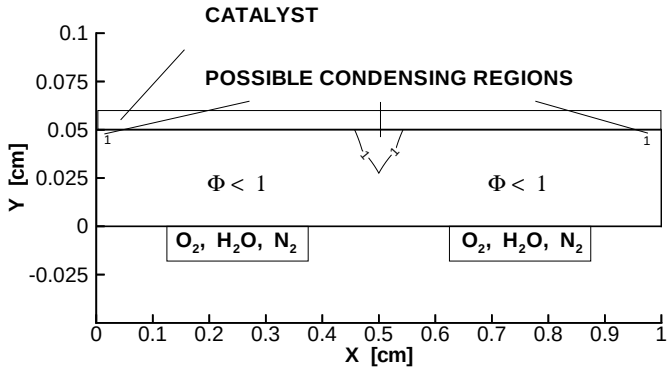

Figure 5: Regions of possible condensation predicted by the model, assuming isothermal conditions.

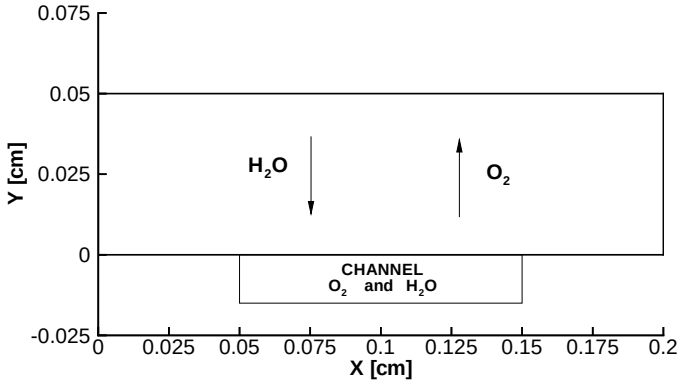

Figure 6: Fuel cell used by Bradean et al. (2001).

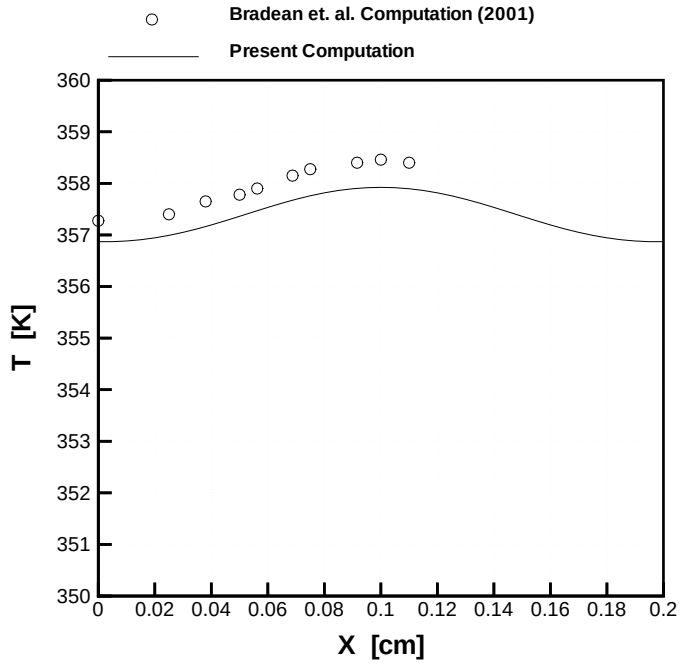

Figure 7: Comparison of temperature distribution at the catalyst boundary (the top boundary) with the results of Bradean et al. (2001).

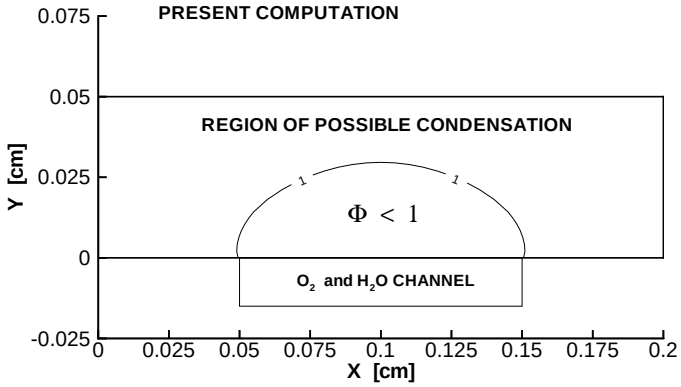

Figure 8: Region of possible condensation predicted by the present two-species non-isothermal computation with one channel.

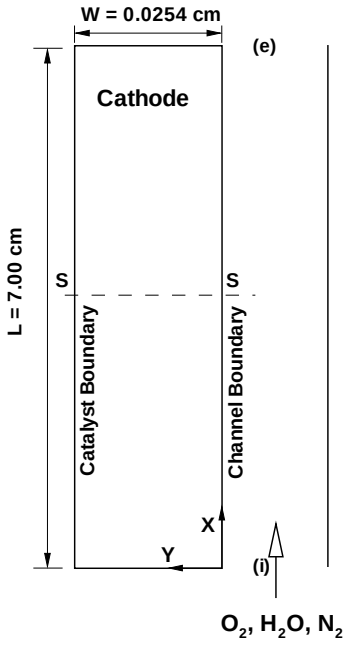

Figure 9: Cathode and channel schematics in Um et al. (2000) computation.

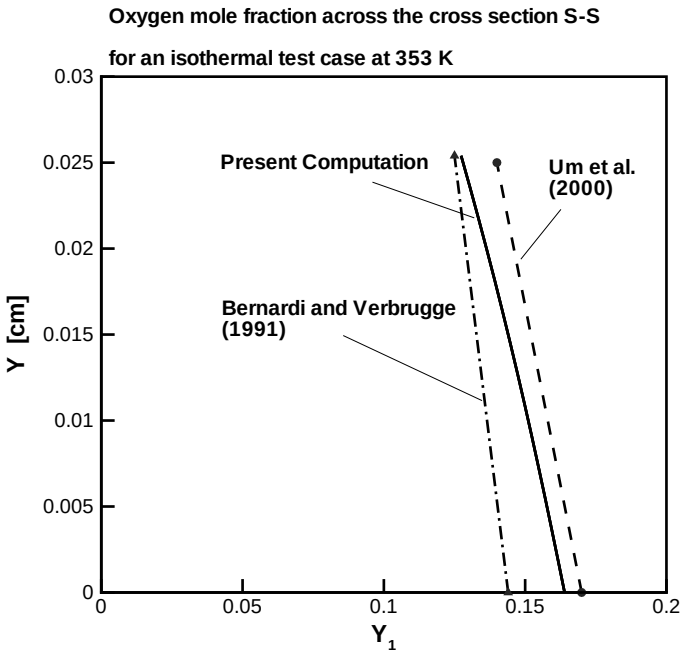

Figure 10: Comparison of oxygen mole fraction (Y_1) across the porous media of cathode, at the cross-section $S-S$ of the previous figure.

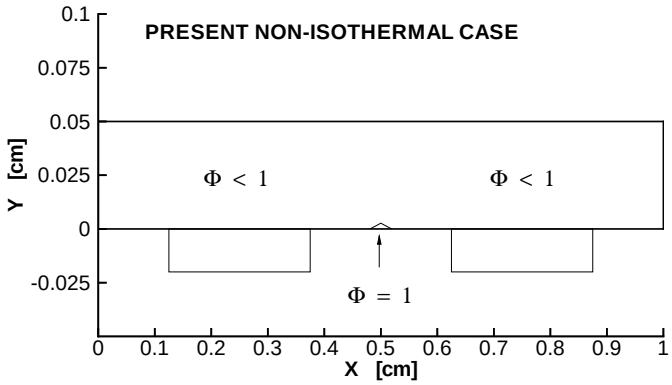

Figure 11: Region of possible condensation predicted by the present three-species non-isothermal computation with two channel.

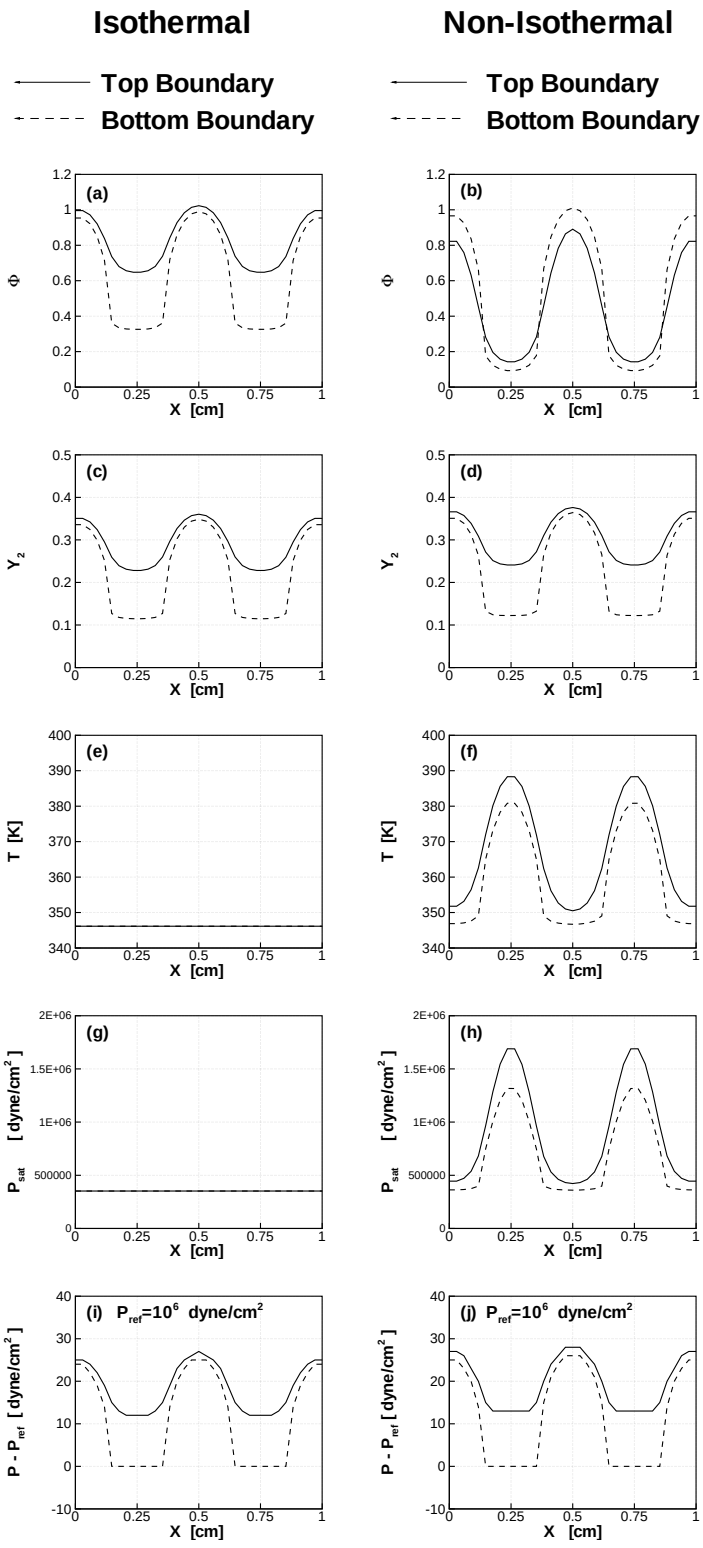

Figure 12: Comparison of three-species isothermal (left) and non-isothermal (right) computations.